

Springtime C-Band SAR Backscatter Signatures of Labrador Sea Marginal Ice: Measurements Versus Modeling Predictions

Charles E. Livingstone, *Member, IEEE*, and Mark R. Drinkwater, *Member, IEEE*

Abstract—During the March 1987 Labrador Ice Margin Experiment (LIMEX '87) two independent investigations were conducted to determine the C-band backscattering cross section of the marginal pack ice along the Newfoundland coast. In one experiment, data from a recently calibrated C-band airborne scatterometer were combined with C-band synthetic aperture radar (SAR) data to measure the normalized scattering cross section of the ice from 10° to 74° incidence angle to within ± 2 dB. In the other experiment, detailed measurements of ice surface roughness and surface properties were made and the radar cross sections were predicted from a scattering model. This paper combines measured and model results and shows them to be fully compatible. By extension, this study is expected to apply to any rubble sea-ice surface when surface scattering dominates.

I. INTRODUCTION

THE SEASONAL sea-ice pack along the Labrador and Newfoundland coasts has a major effect on the local marine industries. In spite of a decade of routine ice reconnaissance by airborne imaging radars, very little quantitative data on the microwave signatures of sea ice existed for this region prior to the LIMEX '87 experiment in March 1987. Previous studies of Labrador/Newfoundland pack ice [1], [2] were conducted north of the LIMEX experiment area in winter conditions, and the early work [2] was qualitative in nature.

The ice pack in these regions is subjected to extremely variable wind, wave and temperature conditions during its growth, and southward advection, with the result that the basic structural elements of the pack are small (typically less than 20-m diam.) cakes of predominantly first-year ice which are extensively deformed and rafted. Depending on the air temperature and degree to which a particular area is sheltered from wave action, the ice cakes may be freely moving with the ocean surface or may be frozen together into large, structurally fragile composite floes. General pack-ice conditions present during the LIMEX '87 experiment are described in overview papers by Carsey *et al.* [3], Drinkwater and Digby-Argus [4], and Digby-Argus and Carsey [6].

With the advent of the ERS-1 (1991) and Radarsat (1994) spaceborne SAR it will be possible to make routine observations of the eastern North American pack ice. In order for this data to be operationally useful to the marine industries, the re-

lationships between the radar reflectivity of the ice, its concentration, and its surface characteristics must be known. Models are required to infer the ice surface conditions from the statistics and spatial distribution of the radar returns that form a SAR image.

During the LIMEX '87 program two independent experiments were conducted to determine the radar-scattering signatures of the ice pack. One experiment measured the spatial distribution of the normalized scattering cross section of the ice by means of an airborne SAR and a calibrated fan-beam scatterometer. The other experiment directly measured various surface properties, including the roughness of the ice using a profiling roughness gauge operated by surface parties, and inferred the scattering cross section of the ice by means of a relatively simple model [5].

This paper presents results from both experiments and combines them to show that a reasonable, tractable scattering model does indeed exist for this ice pack. Finally, the model is inverted in such a manner that when fitted to the observed SAR and scatterometer signatures it can be used to infer the surface properties of snow-covered ice under spring conditions.

II. SURFACE MEASUREMENTS AND AIRBORNE DATA ACQUISITION

A. Ice Surface Conditions

During March 1987, sea ice became compacted against the eastern coast of the Avalon Peninsula, Newfoundland, under the forcing of atypical, unseasonal southeasterly winds. This sudden and vigorous compaction event began on 16 March, but eased somewhat with a combination of swell penetration and a shift to predominantly northeasterly winds on 21 March. The direct consequence of this ice compaction process was a relatively well-fractured and deformed pack consisting of large, seemingly rigid composite floes formed of small floes or cakes frozen or mechanically held together under ice-pressure conditions.

Previous analyses of LIMEX '87 SAR images have concluded that the ice pack was distinctly nonuniform in its characteristics [5], [6]. Additional airphoto analysis and a combination of floe-size distribution information have led to the delineation of two zones within this marginal ice. These "inner" and "outer" zones are separable on the basis of floe-size distribution statistics and SAR image-intensity characteristics [3]. Floes in the outer zone shown in Fig. 1 were small fragmented cakes less than 15-m in diameter which had bumped together under the influence of swell penetration. As a consequence of the wave motion, these floes have rounded outlines,

Manuscript received November 2, 1989; revised May 2, 1990. This work was supported by the National Aeronautics and Space Administration and by the Canada Centre for Remote Sensing.

C. E. Livingstone is with the Canada Centre for Remote Sensing, 2464 Sheffield Road, Ottawa, ON K1A 0Y7, Canada.

M. R. Drinkwater is with the Jet Propulsion Laboratory, California Institute of Technology, 4800 Oak Grove Drive, Pasadena, CA 91109.

IEEE Log Number 9040203.



Fig. 1. Photograph of outer zone ice conditions on March 23, 1987, taken by M. Drinkwater from the CSS *Baffin*. Large floes in the foreground are around 3–5-m diam. and show signs of rafting, deformation, and levée building.

are often extensively rafted, and have prominent levées (raised edges formed by freezing slush and sea water forced up between floes during collisions) (Fig. 1). In contrast, inner zone floes (often conglomerates of small, rafted ice cakes) showed no evidence of recent destructive wave action, were generally larger (up to 30 m in diam.), and had less surface deformation than the outer zone floes. In addition, the interior floes appear to have a thinner snow cover than was found in the outer zone, and ponding from surface snow melt is more apparent.

B. LIMEX '87 Surface Experiment Sites

Ice surface observations were conducted between 15 and 26 March from the vessel CSS *Baffin* in support of aircraft remote sensing data acquisition flights [3]. The area in which the LIMEX surface-measurement program was conducted lies over the northern section of the Grand Banks, a broad continental shelf off the east coast of Newfoundland. Specific sites at which detailed measurements were made are shown in Fig. 2 in relation to the position of the ice edge. Unfortunately, shipborne work was restricted to the outer edge of the ice, although aerial photo-interpretation (from airborne strip mosaics and helicopter photographs) has given useful insights into the characteristics of the inner zone.

Principal measurements at sites in Fig. 2 included snow and ice physical and chemical characteristics, surface roughness profiles, and weather conditions (see overview in [3]). A photographic record was acquired with site descriptions and general composition and roughness of the ice cover. Detailed surface-roughness profile data were obtained principally on 20 and 21 March in order to acquire information on the wavelength-scale surface attributes which dominate backscattering. The Jet Propulsion Laboratory (JPL) surface profiler instrument enabled detailed measurements over a horizontal distance of 1 m, at a resolution of 0.01 m [5]. Roughness profiles were constructed from overlapping sections along transects of up to 22 m in length. Surface characterization data acquired at the outer ice margin by the experiment group working from the CSS *Baffin* included snow and ice depths and salinity profiles, along with snow density, snow wetness, and temperature measurements.

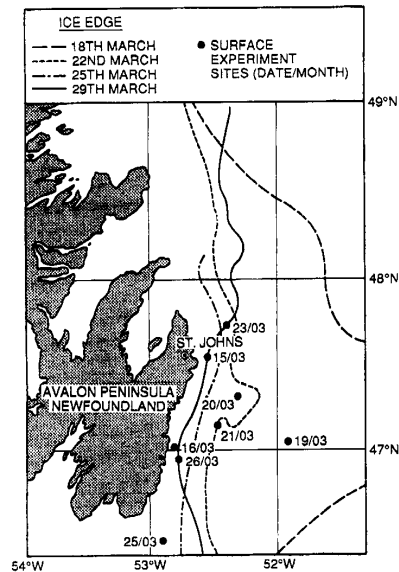


Fig. 2. Location and timing of surface measurements during LIMEX '87 in relation to the ice margin as determined from routine ice reconnaissance flights by the Canadian Atmospheric Environment Service. The data show the positions of the CSS *Baffin* on the indicated data.

Macro-photography of snow grain morphology was obtained by one of the authors with the aid of specialized camera equipment [5]. Local meteorological conditions were monitored by automated weather stations on the vessels CSS *Baffin* and MV *Quest*, and at St. John's.

Throughout the period of 15–16 March, a dense snowcover, with a depth of 7 cm, was observed upon the surface of the sampled ice floes. A detailed discussion of the measured properties of the snow and ice surface layers is provided and illustrated for this period by Drinkwater [5], and so the results are only briefly summarized here. What began as 16 cm of fresh snowfall on 15 March decreased rapidly in depth as the collective processes of destructive metamorphism transformed the layer into a variety of stages of more snow and, in some cases, firm. Snow crystal macrophotographs illustrate that equitemperature and melt-freeze metamorphism rounded the snow grains and bonded them together into clusters. By 23 March, after several cycles of warming and cooling, the ice floes observed had relatively dense damp snow on their surfaces with mean depths of between 1 and 4 cm. Melt drainage had occurred during warm periods on 16 and 18–20 March, and the combination of desalination by gravity brine drainage and flushing by snow melt reduced the sea-ice surfaces to an extremely low salinity ice layer. Ice cores extracted on 23 March indicated upper 10-cm salinities of less than 0.5 ppt [5]. Typical snow parameters measured in the outer ice zone were grain radii of approximately 0.5–1.0 mm, depths ranging from 0–3 cm, densities of 0.4–0.5 g cm⁻³, and snow wetnesses of around 7% by volume fraction.

C. Aircraft Remote Sensing, Data Acquisition

Two flights of the Canada Centre for Remote Sensing (CCRS) CV-580 aircraft were devoted to the C-band backscattering cross-section study of the LIMEX '87 ice pack.

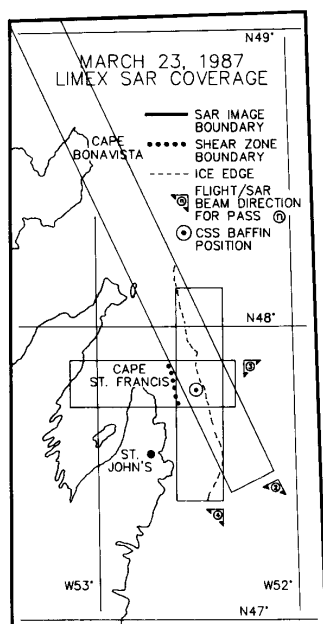


Fig. 3. SAR coverage on March 23, 1987. Three SAR lines were flown on this day, with all three images intersecting over the surface measurement site occupied by the CSS *Baffin*. The SAR image swath width is 9.8 nmi. The locations of the CSS *Baffin*, the ice edge, and the active shear zone are shown. Data from line 3 is analyzed in this paper. Cape Bonavista is labeled to show the location of the March 24 data set.

The March 23 flight was coordinated with surface research activities based on the CSS *Baffin* near the edge of the ice pack east of Cape St. Francis (Fig. 3). Three SAR lines were flown at different aircraft headings so that the intersection of the radar images contained the surface-measurement area during part of the surface activity time window. After the completion of SAR measurements, the aircraft descended to a 302-m altitude and flew a group of three profiling sensor lines within the area imaged by the SAR. Since visibility conditions were favorable, a 9" × 9" format mapping camera was used to acquire photographic strip mosaics of the measurement area during both high-level (photo scale = 1:39 800) and low-level (photo scale = 1:1980) flight lines.

The March 24 dataset was collected in Bonavista Bay (Fig. 4), north of the surface-vessel research area. The dataset acquired contains five SAR image lines organized as two orthogonal mosaics, and nine low-altitude profiling sensor lines which were positioned within the mosaic area. Scatterometer lines were flown over both the pack edge and over the interior region of the ice pack at various track angles spanning 360° to provide data on the aspect sensitivity of $\sigma^\circ(\theta)$ and on the various ice conditions within the pack. Some of the scatterometer data lines were oriented to provide scattering cross-section measurements in the SAR look direction to allow direct correlation of the results from the two sensors. Visibility on March 24 was much poorer than on March 23 and therefore only a limited set of nadir-looking photography was acquired.

For each of the March 23 and 24 datasets, atmospheric and surface conditions were sufficiently stable over the data acquisition periods, so that the SAR and scatterometer measurements within each set can be treated as samples of the same material.

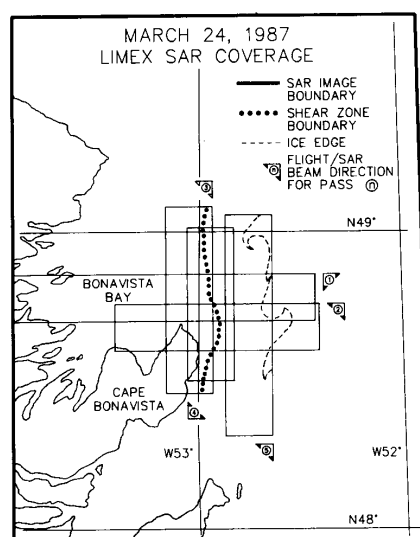


Fig. 4. SAR coverage on March 24, 1987. Five SAR lines were flown to form two orthogonal mosaics of the Bonavista Bay pack ice. SAR lines 1 and 2 form an east-west mosaic of the region; SAR lines 3, 4, and 5 form a north-south mosaic. The SAR image swath is 9.4-nmi wide in each case. Shown on the figure are the ice edge and the edge of the presently active shear zone. The line identification arrows show the flight direction and the radar-look direction.

III. CROSS CALIBRATION OF THE C-BAND SAR AND SCATTEROMETER DATA

A. The SAR System and Its Use for Quantitative Measurements

The architecture of the CCRS radar, details of its controls and data-logging functions, as well as a functional description of this SAR are discussed by Livingstone *et al.* [7], [8].

In principle, the radar equation can be inverted to calculate normalized scattering cross sections $\sigma^\circ(\theta)$ for targets and regions within a SAR-imaged scene from single-look, magnitude-detected or power (squared magnitude)-summed, multilook SAR images, provided that the local incidence angles (θ) are single-valued monotonic functions of the radar slant range (R), as reported by Gray *et al.* [9]. The calculation of $\sigma^\circ(\theta)$ from voltage (magnitude)-summed multilook SAR images such as are produced by most SAR processors is possible under a more restrictive set of conditions and is subject to additional systematic errors since the detected voltage summation process is not energy conservative. For distributed targets such as are found in the LIMEX '87 dataset, the imagery produced by the "real time" processor (looks summed in magnitude) in the CCRS C-band SAR can be used to compute $\sigma^\circ(\theta)$ of a surface if the following constraints are valid: (a) The surface being measured can be approximated as a plane earth; (b) the surface being measured can be approximated as an ideal distributed target; (c) the aircraft altitude is known to within $\pm 0.5\%$; and (d) the surface illumination is not perturbed by radar-motion artifacts. All of these conditions are met reasonably well in the March 23 and March 24 LIMEX '87 datasets.

Independently of the look-summation process used in the radar system, the evaluation of $\sigma^\circ(\theta)$ from radar images requires that: (i) The radiated power is stable and accurately known; (ii)

the radar gains, including the two-way antenna gain function, are stable and accurately known; (iii) the radar receiver and signal-processing components are operating in their linear range; (iv) the models used to account for the imaging geometry, the radar's signal-conditioning functions, the scene illumination (radiated power density over the terrain surface), and the terrain elevation distribution are accurate representations of the conditions present during data acquisition.

Synthetic aperture radar images are formed by two-dimensional matched filtering of phase-coherent raw radar returns accumulated over the time interval by which an element of the imaged surface is illuminated by the radar beam. The matched filters redistributed the temporally and spectrally spread energy from the radar-range chirp and azimuth (along-track) Doppler history to generate spatially registered measurements of the signal returned from each point in the imaged terrain. Each of the "range" and "azimuth"¹ matched filters thus has an associated energy redistribution (compression) "gain" which relates the magnitude of each point in the focused image to that of the raw returns per radar pulse. In the special case of ideal distributed targets that are spatially larger than the surface area whose radar returns are present in the receiver in one inverse band width interval (the "instantaneous" received power from the "real aperture" of the radar), the range and azimuth compression gains are unity. In this case, the "powers" measured at each point in the image can be simply related to corresponding instantaneous received power from a single radar pulse.

The output image power I^2 (where I is the magnitude of the focused radar return) of any pixel in a SAR image is properly expressed in terms of weighted integrals over the radar's aperture to combine the range and azimuth focusing operations with the surface-illumination distribution. For the special case previously noted to be applicable to the March 23 and March 24 LIMEX '87 data, the spatially averaged image power (per pixel) within a real aperture can be expressed in terms of the instantaneous received power at the input to the radar weighted by the total system gain and processing efficiency.

For SAR systems such as that used by the Canada Centre for Remote Sensing (CCRS), which employ a sensitivity-time control to match the systematic part of the dynamic range of the received signal to that of the analog-to-digital convertors (ADC), the relationship between the dynamic, range-normalized, average image intensity and the radar parameters for the plane-earth ideal-distributed target case can be approximated by:

$$\frac{\langle I^2 \rangle}{I_0^2} = \frac{\lambda^2 P_i \beta g_{\text{sys}} \eta \phi c \tau / 2 g_{\text{STC}}}{(4\pi)^3 L_{\text{sys}} e^{2\alpha R} P_{\text{SAT}}} \cdot \left(\frac{R_M^3 \sin \theta_M G_T(\theta - \theta_0) G_R(\theta - \theta_0) \sigma^\circ(\theta)}{R^3 \sin \theta G_{\text{TM}}(\theta_M - \theta_1) G_{\text{RM}}(\theta_M - \theta_1) \sigma_M^\circ(\theta_M)} A_1 \right) \quad (1)$$

where

- $\langle I^2 \rangle$ average pixel intensity of a distributed target averaged over a region centered at slant range R and incidence angle θ ,
- A_1 terrain area corresponding to the image area used to average I^2 ,
- I_0^2 maximum image intensity allowed by the SAR image processor for a distributed target whose

¹We will confine ourselves to simple range-Doppler processing. The complexities of squinted SAR's and spot-light SAR's add nothing to the following arguments.

input signal spans the dynamic range of the ADC,

- λ radar wavelength (m),
- P_i peak transmitter power,
- g_{sys} total gain of the radar receiving chain,
- L_{sys} total signal transmission path loss in the antenna feed lines and radome,
- $e^{2\alpha R}$ two-way atmospheric loss term,
- $R\Phi c\tau/2$ portion of the real aperture of the SAR at range $R(m)$ that has been processed to form the image,
- Φ two-way, processed azimuth beam width in degrees,
- c velocity of light ($m\ s^{-1}$),
- τ range chirp duration (s),
- G_T, G_R gains of the transmitting and receiving antennas,
- $G_{\text{TM}}, G_{\text{RM}}$ model antenna gains used by the radar STC,
- θ radar incidence angle at the resolution cell at slant range R ,
- θ_M plane earth model incidence angle in degrees at slant range R_M ,
- θ_0 elevation bore-sight angle in degrees of the radar antenna,
- θ_1 model antenna bore-sight angle in degrees used by the STC,
- $\sigma^\circ(\theta)$ normalized scattering cross section of the distributed target element at range R and incidence angle θ , and
- $\sigma_M^\circ(\theta_M)$ terrain model normalized cross section.

$$g_{\text{STCmax}} = \left[\frac{R_M^3 \sin \theta_M e^{2\alpha R_M}}{G_{\text{TM}}(\theta_M - \theta_1) G_{\text{RM}}(\theta_M - \theta_1) \sigma_M^\circ(\theta_M)} \right]^{-1} \quad (2)$$

$$R_{\text{min}} < R_M < R_{\text{max}}$$

- P_{SAT} maximum signal power (W) within the range of the analogue-to-digital converter,
- $\langle \rangle_{A_1}$ azimuth-weighted (by the azimuth antenna pattern) average of the bracket contents over azimuth angle Φ and the range interval defined by the image intensity averaging region,
- η radar data-processing efficiency (fractional beam width processed, range and azimuth weighting losses, ADC conversion losses, etc.), and
- β look summation factor that compensates for the look image weighting imposed by the azimuth antenna gain as well as the look summation law used. For the CCRS SAR real-time processor which produces multilook imagery by summing look image magnitudes

$$\beta = \left(\sum_{i=1}^7 \sqrt{P_i} \right)^2 / \sum_{i=1}^7 P_i$$

where P_i is the power in the i th look image.

For the image geometry, radar settings, and targets in the LIMEX '87 March 23 and 24 flights, we can rewrite (1) as:

$$\sigma_{\text{SAR}}^\circ(\theta) = \frac{1}{BL} \sum_{i=K}^{I+K} \left(\frac{1}{T} \sum_{j=S}^{S+T} \left(\frac{N_{ij}^2 - b^2}{(256)^4} \sigma_M^\circ(\theta_{Mj}) \right) \right) \quad (3)$$

$$= \frac{1}{B} \frac{\langle I^2 \sigma_M^\circ(\theta_M) \rangle}{I_0^2}$$

where $I_{ij}^2 = N_{ij}^2 - b^2$, and N_{ij} is the magnitude of the i, j th real-time processor output pixel contained in the azimuth interval $K \leq i \leq K + L$ and in the range interval $S \leq j \leq S + T$; “ b ” = 18 is a processor artifact that existed at the time of the LIMEX '87 data acquisition. For the application of (3), T is chosen so that the azimuth interval averaged exceeds one synthetic aperture length; L is normally chosen in the range $1 \leq L \leq 8$.

The STC terrain scattering model used during LIMEX '87 was $\sigma_M^s(\theta_M) = (-2.173 - 0.2197 \theta_M)$. “ B ” is nominally a constant for each radar operating state, except for range-dependent mismatches between the STC geometry and imaging geometry, and contains the remainder of (1).

The radar-scattering cross-section estimates $\sigma_{\text{SAR}}^s(\theta)$ produced by evaluating (2) are related to the terrain-scattering cross section:

$$\sigma^s(\theta) = \sigma_{\text{SAR}}^s(\theta) \xi(\theta). \quad (4)$$

$\xi(\theta)$ is a residual error term which includes all systematic errors in the radar parameters as well as low-level interferometer modulation produced by antenna/airframe multipath geometry (this effect is found in most airborne synthetic aperture radars). The key SAR parameters for the analysis of LIMEX '87 March 23 and 24 data are shown in Table I.

B. The Scatterometer System

The CCRS CV-580 carried two fanbeam scatterometers during LIMEX '87: A Ku-band instrument operating at 13.3 GHz and a C-band instrument operating at 5.7 GHz. The antennas for both scatterometers are hard-mounted to the airframe so that the broad patterns of the antennas ($+60^\circ$ to -60°) are aligned with the body axis of the aircraft. Each scatterometer has four antennas: H transmit, H receive, V transmit, and V receive and radiates a selected polarization as a high-purity CW signal. Both polarizations are received simultaneously. During data acquisition the scatterometer measurement swath is defined by the aircraft altitude and the cross-track antenna beam width. Along-track resolution is achieved by Fourier transforming and filtering the Doppler-shifted received signals. The incidence-angle dependence of the radar returns is calculated from the scatterometer measurement geometry using simultaneously recorded time histories of the aircraft velocity vector and attitude as well as radar altimeter measurements.

The scatterometer gain is continuously monitored by calibration side-tones derived from the transmitter output and embedded in the received signal. The principles of operation of the scatterometer and an outline of the data-processing procedures may be found in a report by Livingstone *et al.* [10]. Recent work on scatterometer calibration and a complete bibliography for the CCRS instruments may be found in [11]. A calibration study reported in [11] concluded that the absolute calibration accuracy of the scatterometers was better than ± 1 dB, and the relative calibration over the incidence-angle range 15° to 50° is found to be ± 0.5 dB.

The key scatterometer parameters corresponding to data presented in this paper are listed in Table I.

C. Data Reduction

The SAR and HH polarized scatterometer datasets from March 23 and 24 were spatially registered and partitioned to select SAR image segments that contained range-traveling scatterometer lines: SAR image intersections for crossed lines that

TABLE I
CV-580 SENSOR PARAMETERS FOR LIMEX '87, MARCH 23 AND 24

SAR			
λ	Wave length	0.0566 m	
η	Processing efficiency	0.381	
β	Look sum correction	6.76	
θ_6	Two way -6 dB beam width	3.6°	
τ	Chirp length	7.0 s	
G_{sys}	System gain	105.6 dB	
L_{TL}	Transmission line losses	-2.4 dB	
L_{RAD}	Radome loss	-2.0 dB	
L_{ATM}	Atmospheric loss	-0.1 dB	
		March 23	March 24
P_t	Peak Pulse Power	603 W	550 W
G_{STC}	STC gain	-92.7 dB	-93.6 dB
H	Altitude	6066 m	3048 m
θ_N	Near swath incidence angle	45°	45°
θ_F	Far swath incidence angle	75.9°	81.5°
	Polarization analyzed	HH	HH
Scatterometers			
		C-Band	Ku-Band
Frequency		5.70 GHz	13.30 GHz
Transmitter power		5 W	1.5 W
Cross track beam width		1.63°	1.5°
Along track beam width		+60°	+60°
Polarization analyzed		HH	HH
March 23			
Operating altitude	Maximum 303 m, Minimum 301 m		
Ground speed	Maximum 92 m/s, Minimum 82 m/s		
Pitch angle	Maximum +3°, Minimum +1.9°		
March 24			
Operating altitude	Maximum 302 m, Minimum 284 m		
Ground speed	Maximum 90 m/s, Minimum 86 m/s		
Pitch angle	Maximum 2.4°, Minimum 1.4°		

contained large areas of similar ice and scatterometer line segments that contained ice whose SAR image signature was uniform. Those image segments that contained apparently uniform ice conditions across the SAR swath were re-scaled to incidence angle using a plane earth model and reduced to $\sigma^s(\theta)$ estimates using (3). The summation ranges used were 100 pixels in azimuth and 2° in incidence angle (translated into slant-range pixels using the mean incidence angle of the selected interval).

Scatterometer data segments were reduced to $\sigma^s(\theta)$ estimates in 5° increments from 10° to 60° incidence angle. These were stored as time histories for scatterometer-SAR data feature comparisons and were block-averaged to produce the best estimates of $\sigma^s(\theta)$ for each ice condition (and in the March 24th dataset for each aspect angle).

$\sigma^s(\theta)$ data were described by linear regressions of $\sigma^s(\text{dB})$ on θ to provide suitable statistics for aspect angle-sensitivity tests and SAR/scatterometer-result similarity tests [10]. Spatially registered SAR and scatterometer $\sigma^s(\theta)$ estimates were plotted on a common scale for display, with no adjustments to either dataset.

IV. OBSERVED BACKSCATTER SIGNATURES

A. March 23, Cape St. Francis

Fig. 5 is a C-band SAR image of the ice pack east of Cape St. Francis on March 23, 1989. On this day the ice surface can be divided into two ice regimes, as discussed above (in Section II-A): (a) An interior ice regime in which sea ice was observed to move slowly southward along the Newfoundland coast over the period March 21 to 26. The ice cover here consists of conglomerate “flocs” that move as integral units until fractured by shear or wave-induced flexural stresses [12]; and (b) an exterior shear zone approximately 10-km wide in which the ice is moving rapidly and within which conglomerate flocs have decomposed into their constituent ice cakes or are in the process of decomposition by wave fracture.

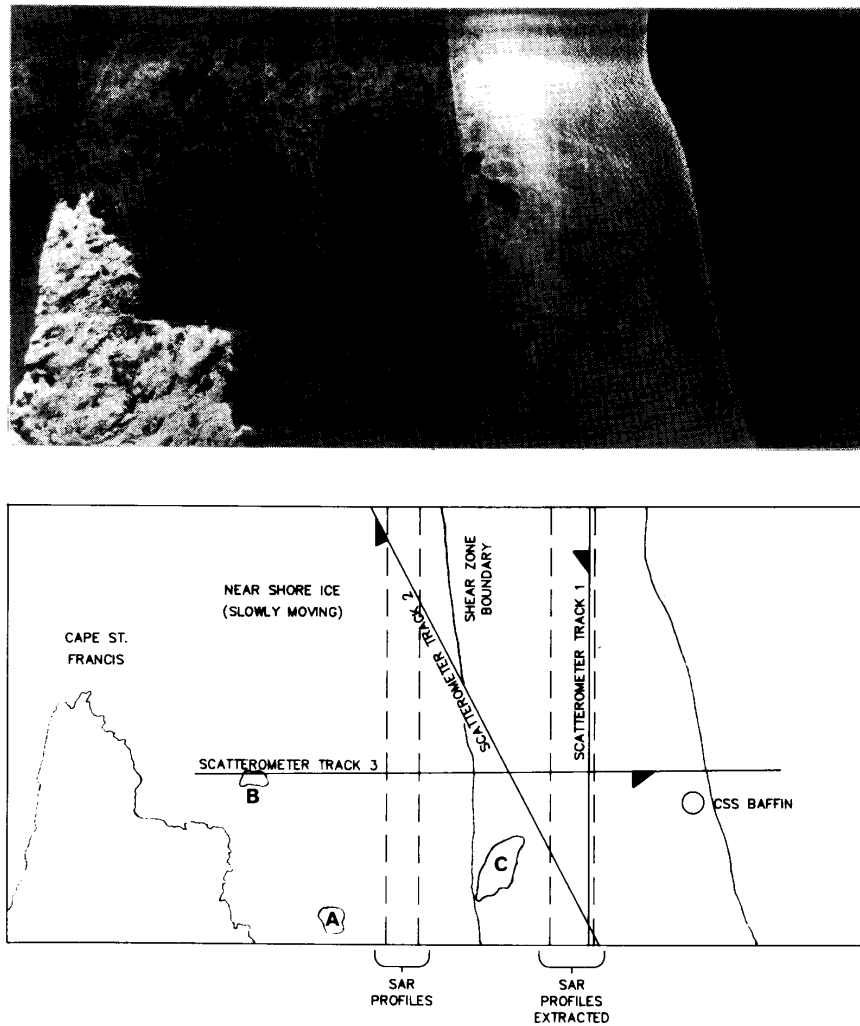


Fig. 5. The SAR scene and scatterometer coverage on March 23, 1987. The image shown is a portion of SAR line 3, including Cape St. Francis and the CSS *Baffin* surface measurement area. The near-range edge of the image (45° incidence angle) is at the top. The CSS *Baffin* is visible in the image as a bright target (in the ice) and its azimuth ambiguity (in the ocean). Clearly visible in the image are the wave-field penetration into the ice, the shear zone, and conglomerate floes in the pack interior. The companion diagram also identifies the scatterometer track positions and the positions of the SAR data samples used in the analysis. The "floes" labeled A, B, and C are conglomerates of smaller ice pans frozen together. Photographic evidence shows the snow cover on these to be saturated with water. The shear zone extends from the shear zone boundary to the ice edge to the right of the image. The image shown is in ground-range presentation, has a width of 9.8 nmi, and spans incidence angles of 45° to 84° .

The shear boundary is sharply defined in the image due to the nature of the differences in the scattering response of these two regimes. The diagram at the bottom of Fig. 5 shows the three scatterometer tracks flown through this area and regions used to extract SAR data for signature analysis.

Scattering cross-section measurements from scatterometer line 1 and from the shear-zone SAR profiles are shown in Fig. 6. Results for scatterometer line 2 and the pack interior-ice SAR profiles are presented in Fig. 7. In both of these graphs the scatterometer data has little incidence-angle-dependent structure, whereas the SAR data contains systematic deviations as large as 1.5 dB from its regression line. A detailed examination of

aerial photographs of the surface corresponding to the scatterometer data sample shows the region to be statistically uniform in floe-size distribution and surface deformation. The SAR data samples used for σ° estimations were extracted from a larger spatial area (Fig. 5) which contained regions of varying floe-size distribution. Since in SAR imagery of sea ice a radar return profile in the range direction has a one-to-one mapping between the range and incidence angles, the range-direction surface-roughness variations are observed as variations of σ° with incidence angle. In addition to σ° variations with the ice surface, Figs. 6 and 7 also contain small (<0.50 dB) contributions from the systematic error term $\xi(\theta)$ (equation (4)) in the incidence

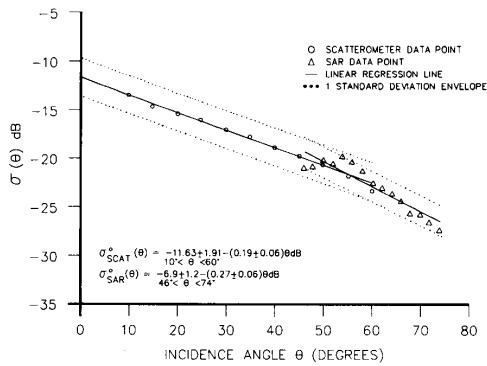


Fig. 6. Shear-zone scattering cross section on March 23, 1987. The curve presented is a superposition of data from C-band scatterometer track 1 and a shear-zone-range scan of the C-band SAR data. Each dataset is characterized by a linear regression line of the scattering cross section in dB and incidence angle. The structure of the SAR data (deviations from the regression line) is spatial trends in ice cross section due to spatial variations in surface deformation in the shear zone. (HH polarized.)

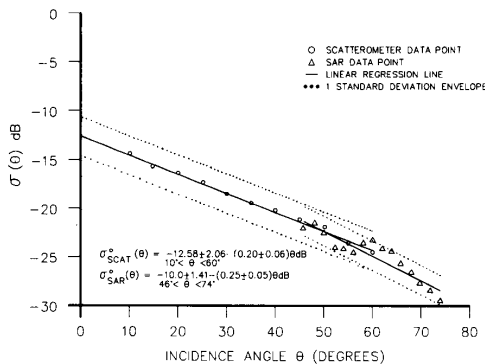


Fig. 7. Pack interior scattering cross section on March 23, 1987. SAR and scatterometer data are superimposed on the same graph to define the C-band scattering cross section-incidence angle relationship for ice in the pack interior. Each dataset is characterized by a regression line. The deviations of the SAR sample points from the line are real spatial features of the pack ice that are located at the incidence angles shown. (HH polarized.)

angle range of 45° to 60° due to the antenna-airframe interferometer effect mentioned previously. The regression line is an ensemble average of several closely spaced 300-pixel-wide range transects through the SAR image and is representative of the average ice signature.

A comparison of the regression lines for Figs. 6 and 7 shows that the mean cross sections of the ice over the SAR-image incidence-angle range are 2 dB larger in the shear zone than they are in the pack interior. The signature transition occurs abruptly at the shear-zone boundary (Fig. 5).

Although no direct surface measurements were made in the pack interior region because the surface measurement parties were constrained to work in close proximity to the research vessel *CSS Baffin*, low-level aerial photography acquired along scatterometer track 3 forms a strip mosaic extending from the near-shore region, across the shear zone near the *CSS Baffin* measurement area and into the ocean beyond. The photo mosaic permits observation of surface features with a dimension greater

than 1 m and provides some record of the surface appearance of the ice from the surface measurement site to the pack interior. Since the conglomerate floes are composed of rafted ice cakes, the surface structure of the inshore region is visually (from aerial photos) very similar to that of the outer region (shear zone) except for some evidence of melt pond formation in the vicinity of the darker "floes" in the SAR imagery (for example, Fig. 5, floe B). A count of ice cakes [3] along track 3 shows that the density of 2- to 7-m diam. cakes is largest in the shear zone (peak values of $148/\text{km}^2$), and smallest in the pack interior ($19.6/\text{km}^2$). The ice-cake density declines sharply at the shear boundary. The density of ice cakes with diameter greater than 17 m is uniform over the pack at $0.196/\text{km}^2$.

B. March 24, Bonavista Bay

In the Bonavista Bay SAR mosaic on March 24, 1987 the shear zone is wider and more complex than at Cape St. Francis on the previous day. The active shear region corresponds to the ocean-swell penetration distance of 15.4 km from the open ocean. Shorewards of the shear (outer) zone the entire ice pack moves slowly at rates of the order of 1 km/day, and there is some evidence of differential flow rates [12].

Scatterometer tracks flown on March 24 were configured to sample the uniformity of the scattering cross-section/incidence angle relationship both spatially and as a function of the aspect angle. Fig. 8 is a cluster plot of scatterometer signature-regression coefficients for track headings of 48° , 88° , 173° , 222° and 278° for which the processed data segments are clustered in a single region of the ice pack for all angles. Samples from different pack regions for headings 278° , 88° , 228° have also been included in Fig. 7 to demonstrate the statistical uniformity of the pack ice scattering signatures. The largest separation of any sample mean from the cluster centroid is less than 60% of the smallest sample standard deviation. The data used to derive Fig. 8, although belonging to different areas within the pack ice, are statistically indistinguishable for the purpose of scattering cross-section computation. There is no aspect-angle sensitivity in this dataset. Because of the mechanically dynamic nature of this region, the distinctions between the active shear zone and the pack interior seen near Cape St. Francis on the previous day are missing in the Bonavista Bay dataset.

The SAR/scatterometer scattering cross-section results for a sample of the Bonavista Bay ice are shown in Fig. 9. Since no regionally consistent differences in the scattering cross section are seen over the experiment area on March 24, a set of four SAR/scatterometer datasets representing the largest spread in conditions consistent with the analysis constraints were superimposed to create Fig. 10. These have been extracted from different regions within the pack and represent different SAR swaths and different scatterometer lines. The elevated SAR cross sections at a 46° incidence angle are a radar artifact caused by multipath interference between signals scattered from the radome mount on the aircraft and direct returns from the ice surface and are accounted for by $\xi(\theta)$ in (4).

C. Discussion of Results

A comparison of the March 24 scattering cross-section measurements (Fig. 10) with March 23 results (Fig. 6) shows that the March 24 σ^0 measurements are consistently larger and that the regression line slopes are statistically the same. No surface measurements are available for Bonavista Bay and all surface conditions must be inferred from aerial photographs, Atmo-

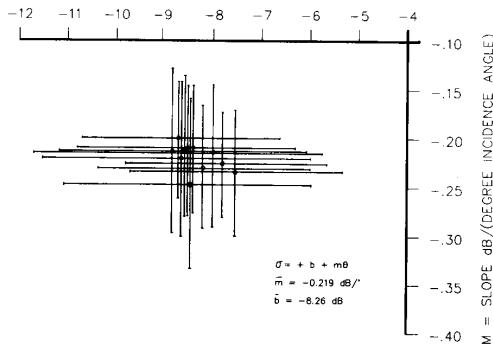


Fig. 8. Regression coefficients cluster plot for March 24, 1987 scatterometer data. The tightly grouped points on the upper left-hand portion of the cluster are samples of ice from the same region of the pack at scatterometer track headings of 48°, 88°, 173°, 222°, and 278°. The remainder of the points are samples from well-separated regions within the Bonavista Bay ice pack. Note that the largest cluster spread along either axis is less than the smallest point standard deviation. $b = \sigma^\circ$ intercept (dB).

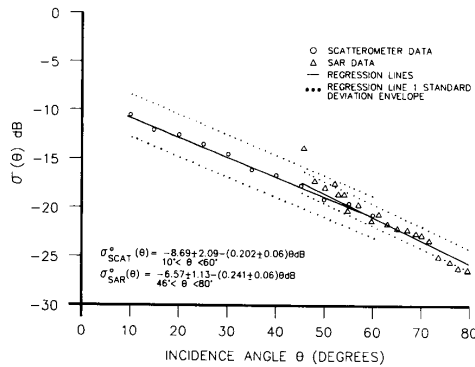


Fig. 9. A typical HH polarized C-band scattering cross-section shear zone near Cape Bonavista versus incidence angle plot from the March 24, 1987 dataset. Both scatterometer and SAR data have been plotted on the same axes. The SAR return at 46° incidence angle is a radar artifact caused by the radome mount interference pattern seen at the top of Fig. 5. Because of the lower flying altitude on March 24 (Table 1) and thus the different antenna-airframe angle, the interference pattern peak is much more pronounced. A similar effect is seen in Fig. 10.

spheric Environment Service (AES) ice charts, and local air temperatures and snowfall statistics. At the start of the March 24 acquisition period new ice was observed on recently opened leads, and by the end of the March 24 flight low-altitude flying was curtailed by declining visibility in snow.

A careful examination of the March 23 and 24 data shows that a linear approximation of the σ° versus θ relationship is reasonable for the ice observed over the incidence angle range of 10° to 60°. At incidence angles greater than 70° this approximation breaks down as expected from model results (Section V-D). Previous experimenters [10], [13] have found that the C-band scattering cross section/incidence angle relationship is stable from mid-winter until the early stages of melt. From the Arctic measurements of Onstott *et al.* [13], typical massive (unrafted) first-year ice has a C-band scattering cross section that can be approximated by $\sigma^\circ(\theta) = -5.0 - 0.35\theta$ dB over the incidence angle range of 10° to 60°. In contrast, all of the LIMEX '87 regression results have slopes in the range 0.19 <

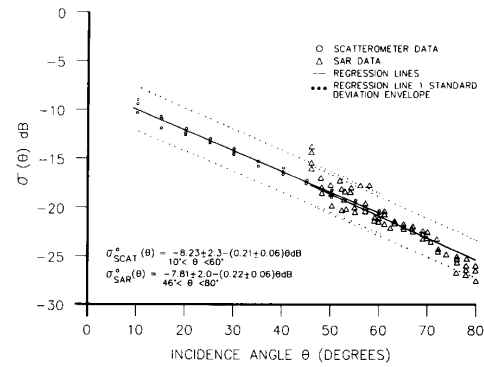


Fig. 10. Composite HH polarized C-band scattering cross section versus incidence angle plot for the March 24, 1987 dataset. Four different $\sigma^\circ(\theta)$ datasets from four different regions in the Bonavista Bay experiment have been superimposed to illustrate the general uniformity of the radar signatures in this area. The regression results presented are for the composite dataset.

$m < 0.25$, which do not come within one standard deviation of the Arctic ice results. Since the material (first-year sea ice) is the same in both cases, and noting the floe count correlation with scattering cross section on March 23, we suspect that the differences between $\sigma^\circ(\theta)$ for LIMEX (broken and deformed) first-year ice and Arctic (massive) first-year ice are explained by surface-roughness elements greater than or equal to 1/4 wavelength (1.4 cm). This is consistent with model calculations based on surface measurements.

V. PHYSICAL OPTICS BACKSCATTERING MODELS

A. Model Formulation

A simple theoretical model has been developed to predict C-band scattering cross sections of pack ice from physical and electromagnetic properties of the snow and sea ice that are readily quantifiable from field measurements. This approach is preferred to the use of more comprehensive (and more complex) theoretical models, since many of these require parameter (and parameter distributions) that cannot be easily measured under field conditions and thus must be inferred from other studies.

Scattering mechanisms for spring snow-covered sea ice studied during LIMEX '87 have been investigated in detail by Drinkwater [5]. An empirical formulation is derived, using basic field-observed surface properties, which may be used to simulate or predict co-polarized (HH or VV) backscatter. This simple model, which is described further in [5], generates a combined external (surface) scattering component and internal (volume) scattering component (from the mean surface property statistics) to give a representative value of the backscatter coefficient (σ°) with incidence angle (θ). The surface-scattering term in the model is based upon the physical optics formulation (for prescribed roughness criteria) which is described elsewhere [14]–[18]. This theory is widely used and is applicable to surfaces with undulations whose average dimensions are large compared with the incident wavelength: Its tacit assumption is that plane-boundary reflection occurs at any point on the surface. In addition to specifying boundary conditions for the surface-scattering term, a standard three-layer or stratified medium is constructed. This simple model design is considered appropriate for spring conditions encountered because penetration

depths are small [5], [12], yet it enables addition of a volume-scattering term to the computed backscatter, if required. In the baseline case the layers consist of air (medium 1), snow (medium 2), and sea ice (medium 3): Separating each layer is an interface where the bulk dielectric properties or physical attributes of the media change.

In general, the like-polarized backscattering coefficient (HH or VV polarization) is composed of both coherent and noncoherent energy. However, the former is only important at near-normal incidence angles, and since we are only concerned with σ° for HH polarization at angles in the range $10^\circ > \theta > 76^\circ$, only the noncoherent component of backscatter is computed. Drinkwater [5] concludes that under the ice conditions observed in the Labrador Sea in March 1987, the principal scattering term is surface scattering and thus the choice of the correct physical optics approximation is critical to the model simulation results.

Roughness statistics obtained during LIMEX '87 [5] highlight two main statistics classes. For the outermost ice floes observed in the vicinity of the CSS *Baffin*, data indicate a normal distribution of random heights, comprising surfaces with either Gaussian or exponentially decaying surface autocorrelation functions. The former is associated with relatively rough deformed ice with rms slope(s) exceeding $s = 0.25$ rad, while the latter is associated with relatively smoother, undeformed ice floe surfaces. The physical optics or Kirchhoff formula is used to simulate surface backscattering from these two classes of surface roughness. In the case of rough ice, a geometric optics or stationary-phase approximation is appropriate providing that validity conditions are met for its application (i.e., $2\pi > 6\lambda$ and $\sigma_h > \lambda/3$) [15]. For smoother exponential surfaces a scalar approximation is applied (i.e., $s < 0.25$) [5], [15]. Both approximations are applicable to surfaces having undulations whose average horizontal dimensions are large compared to the incident wavelength ($\lambda = 0.0566$ m).

In all examples a damp snow layer was observed, and the volume backscatter coefficient of the snow layer is computed. Volume scattering is calculated using a particle-cloud analogy proposed by Attema and Ulaby [19], where snow crystals and free-water inclusions are simulated as a cloud of Rayleigh scatterers suspended in air. This technique is described in further detail in Drinkwater [20].

B. Parameterization Using In-Situ Data

The scattering model is devised such that basic layer properties are specified as parameters. Layer 1 (air) is simply assumed to have a complex dielectric constant of $\epsilon^* = 1.0 - j0.0$. The layer 3 (sea ice) complex dielectric constant $\epsilon^* = 3.1 - j0.01$ is used to simulate typical low-salinity sea ice, based upon dielectric measurements of sea ice with similar characteristics at temperatures close to 0°C [21], [5]. Between these layers is the most critical medium, layer 2 (wet snow), which has four independent parameters. These are: Snow density (ρ_s), snow depth (d_s), snow grain radius (r_s), and volume fraction of free-water (W_w). Boundary roughness conditions at the air/snow interface, for example, are specified as either an rms slope s (rad), or in terms of a standard deviation or rms height σ_h (m) and surface correlation length l (m).

The first process in the model simulates the dielectric properties of the snow (air, ice, and water), given the parameters and a dielectric mixture formula [22]. This technique enables the volume-scattering contribution and the absorption or extinction coefficient [15] of the layer to be estimated. The volume

backscatter term is added to the surface backscatter, from the rough air/snow interface, to give the total predicted backscatter coefficient $\sigma^\circ(\theta)$. In all examples examined, absorption or losses within the wet snow layer are sufficient to suppress any significant surface or volume scatter from the sea ice beneath. Thus, although included in the model formulation, sea-ice volume backscatter is assumed to be negligible during this early melt period.

In order to use the model for simulation purposes, field-measured parameters from 21, 23, and 25 March have been used as scaling parameters. Typical mean surface conditions observed for ice floes at the outer margin of the pack (Fig. 2) are used to obtain a first-order estimate of the scattering signatures [5]. Modeling fits to the data presented in this paper are then achieved by systematic variation and tuning of each of the model parameters within the limits of variability in the surface-measurement data.

C. Model Sensitivity

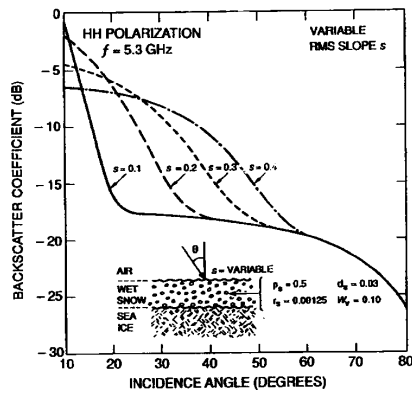
1) *Surface Roughness*: An important feature of this paper is the model response to different surface autocorrelation functions and different slope distributions. Previous statistical work has highlighted two categories of surface roughness classified on the basis of σ_h , l , and s [5]. The Gaussian and exponential correlation approximations to these classes have subtle effects upon the response of $\sigma^\circ(\theta)$ depicted in Fig. 11. The Gaussian backscatter response shown in Fig. 11(a) is typical of that generated with values of rms roughness of $\sigma_h > 1.5$ cm (i.e., approx. $\lambda/4$); layer 2 parameters are indicated. It is an example of a wet, snow-covered, rough-ice floe surface with varying rms slope s , where

$$s = \sqrt{2} (\sigma_h/l).$$

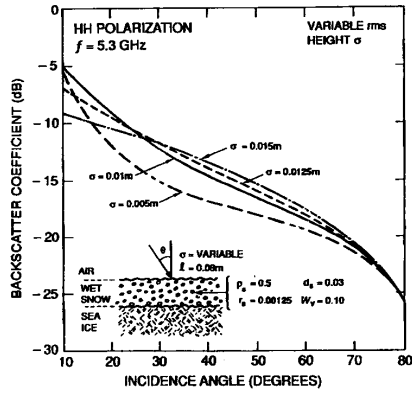
The largest impact upon σ° occurs in the range of $10^\circ < \theta < 60^\circ$, whereupon the gradient of the curve is reduced with increasing roughness. The important feature of curves for values of $0.3 < s < 0.4$ is that they demonstrate an almost monotonic decline with increasing θ .

Using an exponential surface correlation function and scalar approximation for ice floe surfaces with rms slopes of $s < 0.25$, Fig. 11(b) and (c) shows the model sensitivity to σ_h and l using the same layer 2 parameters as in Fig. 11(a). With a fixed correlation length of $l = 8$ cm in Fig. 11(b), increasing σ_h has the effect of reducing σ° between 0° and 20° , while increasing it over the remaining higher incidence-angle range. Reducing l in Fig. 11(c) has a corresponding effect, since it effectively shortens the wavelength of surface corrugations and increases the rms slope. If σ_h is assigned a fixed value of 1 cm, then lowering l from 18 to 2 cm leads to a reduction in $\sigma^\circ(\theta)$ near normal incidence and shallower gradients of $\sigma^\circ(\theta)$ in the range $20^\circ < \theta < 70^\circ$.

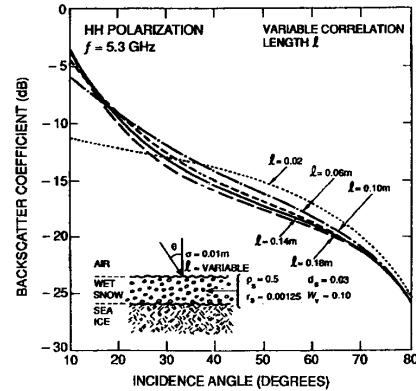
2) *Snow Density and Wetness*: As has been previously shown by Kim *et al.* [23], a snow layer upon sea ice may modulate scattering signatures in a variety of manners. The effects of snow density and snow wetness upon the scattering signature are illustrated in Fig. 12 for an exponential surface with scalar approximation (i.e., $s < 0.25$). Roughness values of $\sigma_h = 1.74$ cm and $l = 12.8$ cm are typical of undeformed, relatively smooth, ice floe surface segments measured in the outer ice zone [5]. Fig. 12(a) demonstrates that an increase in snow density from 0.2 – 0.6 g cm $^{-3}$ causes an increase in the Fresnel reflection coefficient at the air/snow interface. Increased reflectivity raises



(a)



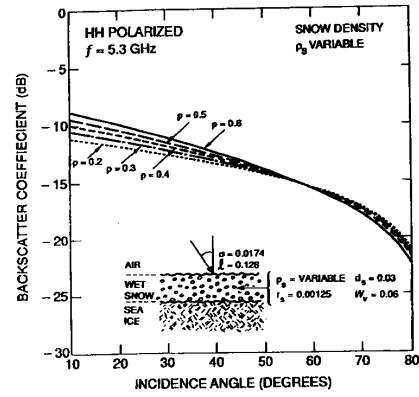
(b)



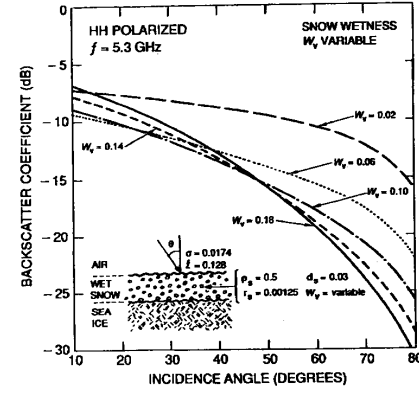
(c)

Fig. 11. Modeled backscatter response to varying roughness scales of wet-snow-covered sea ice with each parameter value indicated: (a) Four variations indicating the effects of different rms slopes upon the signature of a surface with a Gaussian correlation function. (b) and (c) Show the effects of varying σ_h and l upon the signature of a surface with an exponential correlation function.

$\sigma^\circ(\theta)$ near normal incidence, while suppressing it slightly at incidence angles greater than 60° . The variability in $\sigma^\circ(\theta)$ caused by varying snow density, however, is insignificant in



(a)



(b)

Fig. 12. Modeled backscatter response to varying snow parameters for a fixed-surface roughness and exponential autocorrelation assumption. (a) Variations due to snow density ρ_s . (b) Variations due to volumetric fraction snow wetness W_s (%).

comparison with that due to changes in snow-water content. Fig. 12(b) indicates that changes in the scattering signature can be dramatic as a direct consequence of varying snow wetness. When wetness is as low as 2%, the curve has a peak value close to -7 dB and an extremely gradual decline, owing to volume scatter in the snow layer and ice surface scatter. As W_s increases by 4% to 0.06, layer 2 volumetric effects are suppressed by a rapidly increasing extinction coefficient, and σ° is reduced by 2.5 dB. Beyond a threshold of around $W_s = 4\%$, volume backscatter becomes negligible and the original reduction of $\sigma^\circ(\theta)$ in the range of 0° – 30° incidence angle is counteracted by raised surface reflectivity due to snow wetness (and the concurrent increase in the relative permittivity and loss of the snow). The result is a general steepening of the curves, increasing $\sigma^\circ(\theta)$ near-nadir and reducing it at angles over 45° .

D. Comparison Between Simulated and Measured Signatures

Model fits were conducted using the SAR and scatterometer data collected on 23 and 24 March, 1987, presented in Figs. 6, 7, and 9. The technique used is that which was previously explained in Section V-B, and parameters measured on 21 and 23 March were used to obtain an untuned first-order fit to the data.

Since in all cases first-order fits were extremely good when using mean measured snow and ice properties from the measurement sites, there is a high degree of confidence in the final results shown in Fig. 13.

A scalar approximation and exponential correlation function is required in the case of predicting the mean signature of the outer pack on 23 March. Fig. 13(a) shows the fit to the mean 23 March shear-zone signature data in Fig. 6; and the model curve remains within the approximate ± 2 dB standard deviation envelope of the linear regression line, indicating that it is within the confidence limits of the radar data. The predicted roughness statistics are an rms height $\sigma_h = 0.015$ m and correlation length $l = 0.08$ m. Notably, this ice had undergone wave fracture and collisional deformation (see Fig. 1), and these values of σ_h and l are typical of medium rough floes measured in this location [5]. The snow parameters infer a mean surface with almost identical characteristics to those measured on 21 and 23 March. A snow cover under 5-cm depth was observed on these dates, whose mean grain diameter was around 2 mm and whose mean density was approximately 0.5 g cm^{-3} . Although the only detailed snow wetness measurements (made on 20 March) had indicated values of 7% or more, air temperatures fell and remained below the freezing point between 21 and 23 March, enabling snow liquid-water refreeze or drain. A low value of $W_v = 4\%$ also suggests that the upstanding, ridged, or rafted blocks or raised floe edges, which are dominant in the scattering process, are better drained than flat floe surfaces.

The mean signature from the interior ice zone on 23 March (Fig. 13(b)) shows a similar gradient though lower values of $\sigma^\circ(\theta)$ across the whole incidence angle range. The model fit again required a scalar approximation and exponential correlation assumption in order to fit these radar points, and the curve falls within 1 or 2 dB of the measurements. The surface roughness inferred from the fit denotes an rms height of $\sigma_h = 1.75$ cm and correlation length of $l = 12.0$ cm; and these values are consistent with roughness statistics obtained from only the smoothest portions of shear-zone floe surfaces. In contrast, the indicated snow depth is 0.5 cm, with slightly lower density and grain diameter, and a volume fraction of 4.5% liquid water. Although no surface measurements were obtained from the inner ice zone, the low-level aerial photography provides information which corroborates these observations. Certainly floes appear larger, smoother, and relatively less deformed than in the shear zone. Ice surfaces also appear patchy with a mixture of grey tones, indicating that prior ablation had thinned the snow layer, melting down to bare ice in places and leaving some melt ponds. This observation, and the slightly higher inferred snow wetness, is consistent with the fact that these more expansive and exposed surfaces are relatively less-well shadowed from the sun than in deformed ice areas.

The final model fit is performed using the 24 March radar data from Cape Bonavista ice (Fig. 13(c)). Since there was no surface-data collected in that locality, the model is used in a predictive capacity without guidance from local surface data. The backscatter signature is around 2-dB higher than that encountered for the 23 March shear-zone ice and may be explained by the fact that swell waves had recently penetrated and broken up the pack ice. The model prediction required a Gaussian autocorrelation function and geometric optics approximation before achieving the fit in Fig. 13(c). An rms slope of $s = 0.38$ rad predicted by the model implies a surface which is equivalent to the roughest floe surface measured in the Cape St. Francis shear zone (having values of $\sigma_h \approx 0.048$ m and $l \approx$

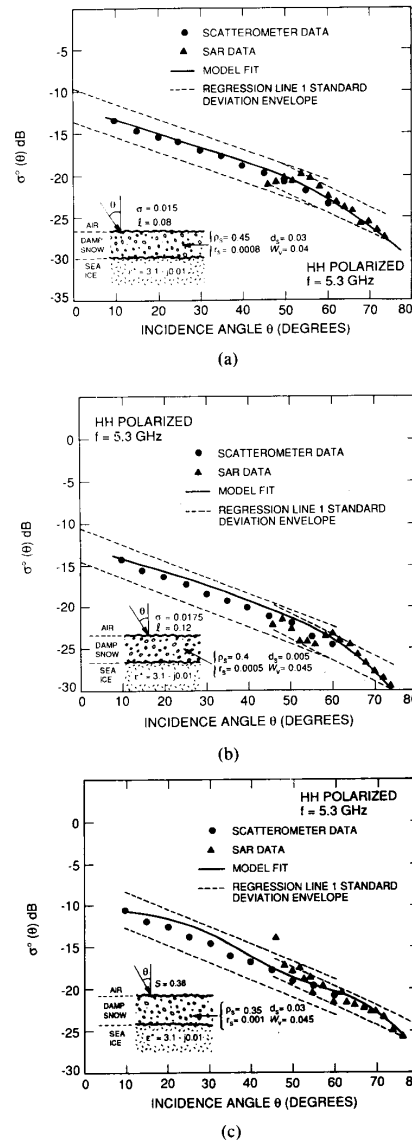


Fig. 13. Model fits to LIMEX '87 radar signatures on March 23 and 24, 1987 with predicted snow properties and roughness values. (a) Model fit with a Gaussian distributed damp snow surface to the shear-zone ice signature from March 23. (b) Model fit with an exponentially distributed damp snow surface to the interior zone signature on March 23. (c) Model fit with a Gaussian distributed damp snow surface to the shear-zone signature from Bonavista Bay on March 24.

0.18 m [5]). This is supported by the observation of new wave fracture and flexural or collision-induced deformation of ice floes in this region. Temperatures fluctuated around freezing point throughout the day, but below freezing temperatures during the previous night accounted for aircraft observations of new ice in leads. Other than an expected lower value of snow density ($\rho_s = 0.35 \text{ g cm}^{-3}$) due to the recent snowfall, snow parameters are largely similar to those measured off Cape St. Francis on the previous day.

VI. SUMMARY AND CONCLUSION

A calibrated C-band scatterometer and C-band SAR have been used to measure the scattering properties of pack ice in the southern Labrador Sea at the onset of melt conditions. When the distributed target form of the radar equation is inverted to estimate the normalized scattering cross section $\sigma_{\text{SAR}}^0(\theta)$ of the ice, the results fall within one standard deviation of scatterometer measurements, $\sigma_{\text{SCAT}}^0(\theta)$, for the same ice. SAR and scatterometer data can be combined to estimate $\sigma^0(\theta)$ for the LIMEX '87 pack ice over the incidence-angle range $10^\circ \leq \theta \leq 74^\circ$ to within ± 4 dB.

Signature data obtained on 43 and 44 March have been described using linear regression analysis. No aspect-angle dependency is found in the LIMEX '87 marginal ice dataset, and the gradient of the $\sigma^0(\theta)$ curves implies uniform rough-surface scattering as the dominant mechanism. The "correlation coefficients" or gradients are much lower than in first-year ice results from Onstott [13], thus implying that the surface is rougher than has been previously reported from calibrated radar measurements. Measures of σ_h and l in the Labrador Sea [5] indicate that the range of surface roughness previously portrayed in papers by Kim *et al.* and Onstott [13], [17] do not include well-deformed marginal ice. Such examples of extreme, marginal ice zone surface-roughness indicate that Gaussian autocorrelation functions can in some instances be used to explain scattering signatures from recently deformed rough ice (with slopes of $s > 0.45$) in the Labrador Sea.

The simple model used in this paper is demonstrated to have the ability to simulate the measured radar signatures to within ± 4 dB. It combines a number of scattering processes which influence σ^0 , while retaining a minimal number of easily measured parameters. Sensitivity studies along with the fits to the LIMEX data highlight the effects of an important interdependency between surface roughness and snow wetness in these circumstances. Due to snow wetness, penetration is reduced and surface scattering appears to be the predominant mechanism. The type and degree of roughness are the factors which enable a signature distinction between the inner and outer ice regimes on 43 and 44 March 1987. The resulting variability in the radar signatures is of the order of 4 dB or more between the inner and outer zones.

From the modeling results, the slope distribution of the pack ice and wet snow cover is a key parameter in the determination of the scattering signature. As reported in [5], the slope distribution and roughness statistics of the LIMEX '87 pack ice are largely determined by the floe edges, rafted blocks of ice, floe deformation features (e.g., floe levées), and ice and snow surface-roughness elements of dimension greater than $\lambda/4$. Since the density of roughness elements in the pack is inherently linked to the degree of wave penetration and the dynamics of pack-ice break-up, it is not surprising that a relationship is seen between the floe-size distribution and the signatures of the ice as has been reported in [6].

Although the model discussed in this paper was developed for the conditions found in the Labrador marginal ice zone, it should be easily extended to the prediction of signatures of other rough first-year ice (ridges and rubble fields) and of young brash ice bands seen in the Arctic during freeze-up.

In the course of this work we have shown that a simple scattering model based on surface measurement results agrees well with microwave measurements of the sea-ice scattering cross section. To what degree can models of this class be inverted to infer surface conditions from electromagnetic measurements?

The difficulties encountered in making inverse model predictions, using the approach described in this paper, are an obvious restriction. These arise first as a result of the intervention necessary to choose between surface autocorrelation function assumptions, and secondly from requiring a reasonable knowledge of surface conditions before being able to generate a first-order fit to the data. The former problem could be circumvented in certain cases (when $s < 0.3$) by using a surface-scattering formulation which is based upon the surface-roughness spectrum such as the small perturbation theory. In this case, the assumptions are slightly different from the Kirchhoff model in that the surface may vary on horizontal scales less than a wavelength, but for HH polarization the model is mathematically identical in form to the scalar approximation used in this paper. The benefit is that the form of the correlation coefficient is implicit in the roughness spectrum prescribed by the model. An isotropic roughness spectrum, for instance, may be cast in terms of both correlation length and the standard deviation of surface roughness when either a Gaussian or exponential correlation coefficient is assumed.

Finally, in the context of these results it should be added that conditions experienced during LIMEX '87 present a relatively simplified case for modeling. When snow wetness volume fractions are large, volume scattering can be effectively disregarded. Under such circumstances, errors inherent in predicting surface conditions are minimized and appear to result largely from the statistical variability in surface roughness conditions. Nonetheless, backscattering can be biased to a large degree in areas of recent wave fracture; for example, by a few surface elements which are unrepresentative of the mean ice conditions (in terms of their characteristics). More thought needs to go into this notion before geophysical algorithms are devised for extracting ice surface information from satellite radar data. The results of this thinking should ultimately determine "which" as well as "how many" model parameters are successful in describing any given sea-ice surface before model inversion is valuable.

ACKNOWLEDGMENT

The authors would like to acknowledge the efforts of all those involved in the LIMEX '87 project, and especially those involved in surface and remote sensing data acquisition and SAR and scatterometer data processing. MRD performed this work at the Jet Propulsion Laboratory, California Institute of Technology, under a contract with the National Aeronautics and Space Administration, while funded by a National Research Council Resident Research Associateship award.

CEL was the leader of the CCRS project under which the airborne data analysis was performed. The CV 580 data acquisition for LIMEX '87 was directly funded by CCRS.

REFERENCES

- [1] S. A. Digby-Argus, R. K. Hawkins, and K. P. Singh, "Microwave remote sensing of ice in Lake Melville and the Labrador Sea," *IEEE J. Oceanic Eng.*, vol. OE-14, pp. 503-517, July 1987.
- [2] R. D. Ketchum, Jr., "An evaluation of ERIM X-L band airborne synthetic aperture radar imagery of sea ice," NORDA Tech. Note No. 48, July 1978.
- [3] F. D. Carsey *et al.*, "Overview of LIMEX '87 ice observations," *IEEE Trans. Geosci. Remote Sensing*, vol. 47, pp. 468-484, Sept. 1989.
- [4] M. R. Drinkwater and S. Digby-Argus, "LIMEX '87: An inter-

- national experiment in the Labrador Sea marginal ice zone," *Polar Rec.*, vol. 45, no. 155, pp. 335-344, 1989.
- [5] M. R. Drinkwater, "LIMEX '87 ice surface characteristics: Implications for C-band SAR backscatter signatures," *IEEE Trans. Geosci. Remote Sensing*, vol. 47, pp. 501-513, Sept. 1989.
 - [6] S. Digby-Argus and F. D. Carsey, "SAR imagery of the Grand Banks ice pack and its relationship to surface features," in *Proc. IGARSS '88* (Edinburgh, UK), Sept. 14-16, 1988, pp. 1445-1448.
 - [7] C. E. Livingstone *et al.*, "CCRS C-band airborne radar—system description and test results," in *Proc. 11th Can. Symp. Remote Sensing* (Waterloo, ON), June 44-43, 1987, pp. 503-518.
 - [8] C. E. Livingstone, A. L. Gray, R. K. Hawkins, and R. B. Olsen, "CCRS C/X airborne synthetic aperture radar: An R&D tool for the ERS-1 time frame," *IEEE Aerospace and Electronic Systems Magazine*, vol. 3, no. 10, pp. 11-40, Oct. 1988.
 - [9] A. L. Gray, P. W. Vachon, C. E. Livingstone, and T. I. Lukowski, "Synthetic aperture radar calibration using reference reflectors," *IEEE Trans. Geosci. Remote Sensing*, vol. 28, pp. 374-383, May 1990.
 - [10] C. E. Livingstone *et al.*, "The CCRS/Sursat active-passive experiment 1978-1980: The microwave signatures of sea ice," Canada Centre for Remote Sensing, Ottawa, ON, Data Acquisition Div. Rep., June 1983.
 - [11] R. K. Hawkins, P. J. Farris, J. R. Gibson, and K. P. Singh, "Calibration of the CCRS airborne scatterometers," *IEEE Antennas Propagat.*, vol. 38, pp. 903-918, June 1990.
 - [12] M. R. Drinkwater and V. A. Squire, "C-band SAR observations of marginal ice zone rheology in the Labrador Sea," *IEEE Trans. Geosci. Remote Sensing*, vol. 27, pp. 522-534, Sept. 1989.
 - [13] R. G. Onstott, T. C. Grenfell, C. Matzler, C. A. Luther, and E. A. Svendsen, "Evolution of microwave sea ice signature during early summer and midsummer in the marginal ice zone," *J. Geophys. Res.*, vol. 92, no. C7, pp. 6825-6835, 1987.
 - [14] H. J. Eom, "Theoretical scatter and emission models for microwave remote sensing," Ph.D. thesis, Univ. Kansas, Lawrence, 1982, 212 pp.
 - [15] F. W. Ulaby, R. K. Moore, and A. K. Fung, *Microwave Remote Sensing Active and Passive*. Reading, MA: Addison-Wesley, 1982, pp. 457-1064.
 - [16] A. K. Fung and H. J. Eom, "Application of a combined rough surface and volume scattering theory to sea ice and snow backscattering," *IEEE Trans. Geosci. Remote Sensing*, vol. GE-20, pp. 528-536, July 1982.
 - [17] Y. S. Kim, R. K. Moore, R. G. Onstott, and S. Gogenini, "Towards identification of optimum radar parameters for sea ice monitoring," *J. Glaciology*, vol. 31, no. 109, pp. 214-219, 1985.
 - [18] L. Tsang, J. Kong, and R. T. Shin, *Theory of Microwave Remote Sensing*. New York: Wiley, 1985, 613 pp.
 - [19] E. P. W. Attema and F. T. Ulaby, "Vegetation modeled as a water cloud," *Radio Sci.*, vol. 13, no. 2, pp. 357-364, 1978.
 - [20] M. R. Drinkwater, "Radar altimetric studies of polar ice," Ph.D. thesis, Univ. Cambridge, Cambridge, UK, 1987, 231 pp.
 - [21] M. T. Hallikainen, M. V. O. Toikka, and J. M. Hyypä, "Microwave dielectric properties of low-salinity sea ice," in *Proc. IGARSS '88* (Edinburgh, UK), Sept. 13-16, 1988, pp. 419-420.
 - [22] M. T. Tiuri, A. H. Sihvola, E. G. Nyfors, and M. T. Hallikainen, "The complex dielectric constant of snow at microwave frequencies," *IEEE J. Oceanic Eng.*, vol. OE-9, pp. 377-382, July 1984.
 - [23] Y. S. Kim, R. G. Onstott, and R. K. Moore, "The effect of a snow cover on microwave backscatter from sea ice," *IEEE J. Oceanic Eng.*, vol. OE-9, pp. 383-388, Oct. 1984.



Charles E. Livingstone (M'87) received the B.Sc. degree (physics, 1965) and the M.Sc. degree (geophysics, 1967) from the University of British Columbia, and received the Ph.D. degree (physics, 1969) from the University of Western Ontario.

He has worked on the problems in sea ice and ocean remote sensing and on Synthetic Aperture Radar (SAR) development at the Canada Centre for Remote Sensing Ottawa, ON, since 1976. Most recently, he has studied the radio-

metric calibration of SAR systems and their application to sea-ice scattering measurements.

Dr. Livingstone is a member of the Association of Professional Engineers of Ontario.



Mark R. Drinkwater (M'88) was born in Oldham, Lancashire, UK, in 1963. He received the B.Sc. (hons.) degree in physical geography from Durham University in 1984, specializing in remote sensing and glaciology. In 1988 the Ph.D. degree was received from the University of Cambridge in radar remote sensing of polar ice, after completion of a Scott Polar Research Institute thesis entitled, "Radar Altimetric Studies of Polar Ice."

He worked in 1987-1988 as a Research Scientist for Polar Oceans Associates, a UK division of Science Applications Inc., San Diego, CA, before joining the Jet Propulsion Laboratory (JPL), California Institute of Technology, Pasadena, as a National Research Council Resident Research Associate. As a Research Associate (between 1988-1990) he developed techniques in modeling the microwave backscatter behavior of snow and sea ice media. Other focuses involved observing Labrador Sea ice dynamics using synthetic aperture radar data. Recently, he joined the Polar Oceanography Group at JPL as a Research Associate, where his interests include multifrequency polarimetric microwave observations of sea ice and terrestrial ice sheets. His current work is in the development of techniques, including model inversion, for the extraction of geophysical information from satellite microwave data.

Dr. Drinkwater is a member of the International Glaciological Society, the American Geophysical Union, the Oceanography Society, and the Electromagnetics Academy.